Sensing ion channels in neuronal networks with graphene transistors

Farida Veliev, Dipankar Kalita, Antoine Bourrier, Tiphaine Belloir, Anne Briançon-Marjollet, Mireille Albrieux, Vincent Bouchiat and Cécile Delacour[*]

Dr. F.Veliev, Dr. D. Kalita, A.Bourrier, T. Belloir, Dr. V.Bouchiat, Dr. C.Delacour
Institut Néel, CNRS & Université Grenoble Alpes, 38042 Grenoble, France
E-mail: cecile.delacour@neel.cnrs.fr

Dr. A. Briançon-Marjollet
Université Grenoble Alpes, HP2 laboratory, Inserm U1042, 38041 Grenoble, France

Dr. M.Albrieux
Université Grenoble Alpes, Grenoble Institut des Neurosciences, Inserm U1216, F-38000 Grenoble, France

Keywords: ion channel, graphene, grain boundary, neuron, bioelectronics

Abstract. Graphene, the atomically-thin honeycomb carbon lattice, is a highly conducting 2D material whose exposed electronic structure offers an ideal platform for sensing. Its biocompatible, flexible, and chemically inert nature associated to the lack of dangling bonds, offers novel perspectives for direct interfacing with bioelements. When combined with its exceptional electronic and optical properties, graphene becomes a very promising material for bioelectronics. Among the successful bio-integrations of graphene, the detection of ionic currents through artificial membrane channels and extracellular action potentials in electrogenic cells have paved the road for the high spatial resolution and wide-field imaging of neuronal activity. However, various issues including the low signals amplitude, confinement and stochasticity of neuronal signals associated to the complex architecture and interconnectivity of neural networks should be still overcome. Recently, grain boundaries found in CVD graphene were shown to drastically increase the sensitivity of graphene transistors providing nanoscale sensing sites. Here we demonstrate the ability of liquid-gated graphene field effect transistors (G-FET) on which hippocampal neurons are grown for real-time detection of single ion channels activity. Dependence upon drugs and reference potential

gating is presented and is found compatible with the nanoscale coupling of a few ion channels to weak links present in the devices.

1. Introduction

The long lasting interfacing of neurons with electronic devices is of primary interest for a variety of applications in fundamental neuroscience and biomedical engineering. In particular, the implementation of recording devices to probe the activity of neuron-based architectures at the single neuron level is a critical step towards the understanding of the microscopic mechanisms which support information processing, and could eventually offer a valuable tool for in-vivo brain interfacing. Several approaches have been developed to detect the ionic activity of an assembly of neural cells with extracellular micro-electrodes,[1] micro-transistors[2] or silicon nanowires.[3,4] These devices currently provide the best temporal resolution with regards to the deep brain implantation compared to optical or magnetic approaches. However the rigidity and poor acceptance of the devices are main drawbacks limiting this electronic approach. In addition to the poor growth and survival of the cells on the currently used electrode materials, the mechanical mismatch between the rigid implant and the soft biological tissue results in a strong immune response and an increased distance to the cells due to the electrode encapsulation, preventing a close and stable electrical contact to the cells.[5,6]

Recently graphene has emerged as a promising alternative material for biosciences,[7] including interfacing solid-state devices with living cells.[8,9] When compared to mature solid state technologies involving for example silicon or metallic material, critical improvements can be gained using graphene - a single carbon layer - as the bioelectronic sensing interface: its relative chemical inertness to ionic fluids and the absence of dangling bonds together with the existence of a 2D electron gas directly exposed on the graphene surface[10] provide unique

features which should significantly enhance the electrical coupling and the signal-to-noise ratio when associated with the strong adhesion of neurons onto the recording device.[11]

Conventional semiconductors such as silicon nanowires require thick insulating layers (typically 145 nm and 10 nm for bottom and top silicon oxides) to reach the best operating regime and to prevent time aging and degradation of the sensor in reactive liquids. However, because graphene is inert chemically, additional insulating layer is no more required between the transistor channel and the gating liquid. Thus the high mobility regime that can be accessed in graphene with the ultrathin electric double-layers (EDLs) exceeds widely the threshold performance of conventional semiconductor transistors, while keeping similarly high integration and high frequency operation of graphene transistors.[12] Another important aspects are the biocompatibility of graphene[7,45] and its outstanding mechanical properties,[13] which provide sturdy membranes and offers bendability and softness comparable and compatible with biological tissues.[14] The growth of neuronal cells is shown to be significantly improved on graphene compared to silicon or metallic surface: bare graphene exhibits adhesion properties comparable with usual proteins (poly-lysine or laminin) in terms of growth and adhesion of neurons,[11] while preserving the electrical performance of the electrode at the interface to the living tissue.[15] Therefore, the use of graphene for the electrodes material or/and as the surrounding coating leads to an higher density of neurons on the samples and even offers promising perspectives to use similar graphene electrodes for in-vivo recordings. During the past few years, graphene has indeed been shown to be an extremely promising material for neural tissue engineering,[16,17] regenerative medicine[18,19] and was successfully used to record electrical signals from cardiomyocyte cells,[8,9] hinting at the feasibility of a graphene-neuron interface and its possible applications for neural prostheses.[20,21]

Although immunogenicity and toxicity of the implanted graphene[45] have still to be investigated before its used in pharmacology and medicine, CVD-grown graphene

monolayers appear more stable for long term implantation than its counterparts graphene oxide (GO) and reduced graphene oxide (rGO). Macroscale high mobility graphene monolayers can be routinely obtained by CVD growth on Cu foils and then be transferred on a wide range of substrates.[22] However, this graphene unavoidably exhibits a large amount of grain boundaries (GBs) formed by the merging of individual graphene grains with different crystal orientations.[23] These linear defects alter the electronic performance of graphene devices.[24] While many efforts were primarily dedicated to production of large-scale defect free graphene, it appeared that GBs have emerged as highly sensitive line defects for analytic applications. [25,26]

Here, we report on the interfacing of polycrystalline graphene field effect transistors (G-FETs) to hippocampal neurons that are cultured on top, and demonstrate an ultra-high sensitive field effect detection of ion channels activity using graphene grain boundaries. G-FET arrays with varying channel dimensions and varying amount of grain boundaries were fabricated by transferring graphene on glass, on sapphire and on silicon/silicon oxide substrates.

2. Characterization of the Graphene-Field Effect Transistors (GFETs)

Figure 1a provides a schematic equivalent electrical circuit of a G-FET interfaced to an electrogenic cell (inspired from previous work[27]). The ionic current generated by the neuronal activity changes the extracellular voltage V_{extra} in the cleft (the liquid junction formed between the cell and the device which gates the transistors) and modulates the carriers density of the transistor conduction channel as $\Delta n = C_Q.\Delta V_{extra} / q$. GFET are directly exposed to the liquid gate (no top oxide) and thus take advantage of the large interfacial capacitance of the atomically thin electrical double layer *EDL*. The capacitance of the *EDL* takes into account the serial capacitances at the interface, including the quantum capacitance and the geometric (Helmholtz and diffuse) capacitances $C^{-1}_{EDL} = C^{-1}_{Q} + C^{-1}_{G}$. Because the quantum capacitance is

usually the smallest one,[10, 36] its serial contribution dominates the interfacial capacitance such as $C_{EDL} \sim C_Q$ (~2µF/cm²), the Helmholtz and diffuse capacitances being expected to be larger (10-20 and 100-200 µF/cm² respectively). Monitoring the variation of the source drain current $\Delta I_{SD} = \mu.e.\Delta n$ further amplifies the signal by the high carrier mobility μ of the graphene conduction channel. This current signal is usually expressed as function of the transconductance g_m of the G-FET at the liquid top-gate operating setpoint V_G (previously characterized),

$$\Delta I_{SD} = g_m(V_G) \times \Delta V_{extra} \qquad \text{(eq.1)}$$

The amplitude and the shape of the extracellular potential V_{extra} depend on the cell-device coupling strength, the seal resistance, the measured region of the neuron (cell body or neurite) and the amount of voltage-gated channels. The sensitivity of a GFET ($\Delta I_{SD}/I_{SD}$) is usually expressed in term of relative conductance change, given by the transconductance normalized by the drain voltage at the gate operation setpoint V_G :

$$S(V_{SD}, V_G) = \frac{\Delta G}{G} = \left(\frac{g_m}{V_{DS}}\right)\frac{\Delta V_{extra}}{G} = \left(\frac{\partial I_{SD}/\partial V_G}{V_{DS}}\right)\frac{\Delta V_{extra}}{G} \qquad \text{(eq.2)}$$

The normalized transconductance Γ_m (first term of eq.2) being proportional to the device-width to length ratio $\Gamma_m = \mu.C_Q.W/L$, the transistors size can be reduced while keeping high sensitivity in opposition with the microelectrodes (MEA) currently used in electrophysiology and which rely on charge injection mode only.

This general expression (eq.2) holds for a homogeneous electrostatic detection and should be further refined for assessing the non-homogeneous detection generated by the network pattern of highly sensitive grain boundaries in polycrystalline GFET which can probe nanoscale near field emitters[26] such as ion channel. To take into account their contribution, the transistor channel can be described by a repeating unit of single grains *SG* and grain boundaries *GB* which both contribute to the current modulation of the transistor channel:

$$S(V_{SD}, V_G) = \frac{\sum_{N-1} \Delta G_{GB} + \sum_N \Delta G_{SG}}{\sum_{N-1} G_{GB} + \sum_N G_{SG}} \qquad \text{(eq.3)}$$

with N the number of single grain along the GFET channel. Figure 1b shows the non-linear dependence of the normalized transconductance with the device-width to length ratio (inset fig.1b). As expected, the non-homogeneous GB-assisted field effect detection further enhances the sensitivity when the channel length (and thus the number of grain boundaries) is reduced.

The GFETs sensitivity is characterized by applying a DC liquid front gate voltage V_{LG} in the cell culture saline medium surrounding the devices through a quasi-reference Pt-electrode. Figure 1b demonstrates the conductance modulation of liquid gated G-FETs with varying transistor channel dimensions. The dependence with V_{LG} of the current shows a symmetric ambipolar field effect behavior with a (charge neutrality) Dirac point at $V_D \sim 0.4$ - 0.5 V. The normalized transconductance strongly increases when reducing the size of the transistors channel, being the highest (*4 mS/V*) for the smallest devices (10×20 μm²) in agreement with the state-of-the-art.[8,9] These devices also offer a fast response to external potential changes (supporting information figure S2) providing a suitable platform for electrical detection of neuronal activity.

Since few years, intensive studies were dedicated to characterize the grain boundaries of CVD grown polycrystalline graphene by combining atomic force micrograph, Raman mapping and transmission electron micrograph.[26,37] Most impressive results were obtained with dark field TEM analysis which can resolve the grain boundaries over the graphene layer.[23] However it requires see-through samples (graphene membranes) that are not compatible with liquid cell operation. Here we have used alternative methods for mapping the GBs networks which form by the merging of single grain during the CVD growth. In particular, we have analyzed graphene layers (same growth condition) for which the growth has been stopped before full coalescence of the single grains, giving an accurate and large scale evaluation of the nucleation density (figures 1e-f). The grain size can also be assed on the merged graphene layer, by using specific treatments based on an oxidation[40] that

selectively etch the grain boundaries leading to crevasses that can be further imaged using scanning probe microscopy. Both methods agree to give a grain size ranging between 10-30µm (figures 1c-d). Because we are using a pulsed growth process,[29] the shape of the single grain is irregular but still is single crystal. This can be observed also by increasing the time of the growth, because multilayers patches mark the nucleation center of the each single grain.

The main characteristics of the graphene sheet after the device fabrication, such as surface roughness, crystalline quality and electronic mobility, can be seen in the supporting information figure S1. Raman spectrometry analysis (figure S1b) is performed to assess graphene quality. The intensity ratio between the G and 2D bands (resp. 1583 cm^{-1} and 2676 cm^{-1}) I_G/I_{2D} = 0.3 and the width of the 2D-band peak (30 cm^{-1}) match well the values reported for graphene[28] confirming the mono-layer structure of the graphene sheet, while the very low intensity of the D-band peak (1300-1383 cm^{-1}) indicates the low amount of lattice defects. The two-point measurements on graphene stripes with length varying from 50 µm up to 2200 µm show a linear dependence of the device resistance with the probed channel length (figure S1c). The square resistance is geometry-independent and remains constant around $R_{\square}$=0.6 kΩ per square, revealing the overall homogeneity of the graphene material at scales above 50µm. The electronic mobility obtained from back gated field effect measurements is around 6000 $cm^2.V^{-1}.s^{-1}$ (figure S1d), a value consistent with those reported for CVD graphene layers obtained using the same process.[29]

2. Sensing primary neurons with GFETs array

Primary mouse embryos hippocampal neurons were grown for periods of 19-21 days on the different set of G-FETs (see methods). The scanning electron micrograph of the graphene strip performed after the recording shows the presence of well developed neurite network above the sensors (figure 1c). The cultured neurons exhibit a pyramidal shape and highly developed dendritic architecture as well as a dense pre-synaptic markers distribution (figure

1d) as expected for matured hippocampal neurons.[30] Additionally, patch-clamp measurements of somatic spontaneous electrical activity (cell-attached mode) and calcium imaging both show spontaneous activity in these neurons (figure S3) confirming the establishment of operating electrical signaling pathways.

The presence of healthy neurons above the devices is characterized before the measurement with a reflective microscope for the opaque silica substrates. On the transparent sapphire samples (figure 2c), neurons are observed during all the culture time with conventional transmission microscope. The immunofluorescence staining and subsequent fluorescent imaging of the neurons performed after the recordings, provide an accurate mapping of the soma and neurites positions over the transistor channels and confirm their maturation stage (figure 1d, 2a, b, d). The isolating resist layer covers the metallic drain and source contacts (see devices design in figure 2 and in supplementary figure S8), such as more than 90% of the graphene and substrate surfaces are resist-free and therefore exposed to the neural cell media. While a resist-free window located just above the graphene channel could promote suspended neurites above the device, this configuration favors the neurites to spread between the metallic electrodes and adhere on the graphene transistor channel even for the smallest (10x20µm²) GFETs (figure 2d).

2.1. Detection of a random telegraphic signal (RTS)

While graphene transistors with channel dimensions well above the neuron size are unlikely to detect neuronal activity, a significant fraction (33%, 15 tested devices, 2 cultures) of these devices exhibit a particular signal when interfaced to the mature neurons. Figure 2 shows the typical time traces of the square conductivity ($G_{\square}=G/(W/L)=G\times N_{\square}$) obtained on large G-FETs with respective channel sizes of $W\times L$ = 1000×250 µm², 40×250 µm² and 40×50 µm², where W is the width and L the length of the transistor channel. The schematics show the exposed graphene channels (grey), the metallic electrodes (red) and the insulating resist on top (green). The stacked layers (graphene/metal) are also described in supplementary figure S8. The

measured conductance modulation strongly resembles Random Telegraph Signal (RTS or RT signal), which is characterized by time switching between few discrete states, as illustrated by the corresponding conductance histograms. The higher conductance state is attributed to the more occupied ground state, while the lower one represents the excited state (discussed in the next section). While the relative RTS amplitude $\Delta G/G$ increases with decreasing dimensions of the device (figure 2 and 5c), surprisingly the step-like conductance fluctuations were never observed on the smallest fabricated G-FETs with channel dimensions of $W \times L = 20 \times 10$ µm² (blue trace in figure 2d) independently of the neuron seeding density.

The observation of RTS in FETs is usually linked to a finite number of impurities in close vicinity to the conductive channel,[31] which can trap the charge carriers resulting in conductance fluctuations. Upon increasing the number of impurities, random telegraph signals superimpose into a single 1/f noise spectrum. However if only one prevalent impurity is present close to the FET channel, the conductance will fluctuate between two discrete values corresponding to individual trapping/detrapping events. Especially for nanoscale devices, such as silicon nanowire[32,33] or carbon nanotube[34] FETs, where the current is carried by a small number of charge carriers, this will result in a significant change of the channel conductance. This seems to contradict the observation of the extremely high conductance modulation on large graphene transistors ($W \times L \geq 40 \times 50$ µm²). Therefore, we have further investigated the possible source of noise originating from the neurons.

2.2. Impact of drug and neurotoxin on the detected RTS signals

The dynamics of the measured signal clearly depends on the composition of the extracellular medium. While the incubation with bicuculline (BIC, 20 µM, 15 min 37°C) – a $GABA_A$ receptor antagonist which activates spiking activity- results in a large conductance modulation with a switching time varying from few to several hundred milliseconds (black trace in figure 3), replacing the BIC supplemented medium by fresh culture medium decreases the appearance of conductance fluctuations (blue trace in figure 3). Moreover, the subsequent

addition of BIC (during the recording at room temperature) partly reestablishes the conductance fluctuations during the time of recording, and finally the addition of a prominent sodium channel blocker (tetrodotoxin, TTX 0.5 μM) to the extracellular medium completely suppresses the telegraph signal (green and red trace in figure 3 respectively), revealing a clear dependence of the observed RTS on the ion channels activity. The reduced activity after the second injection of BIC could be explain by the several medium changes and the lack of the incubation period (15mins at 37°C) because of the real-time recording, but still it leads to the emergence of a second excited state (inset of the green trace figure 3a). From the recording traces, the low state seems to be associated with the excited state. In the hole operating regime (V_{LG} < 0.4 V) this corresponds to a negative shift of the Dirac point V_D' due to the neuronal activity, implying a positive change of the membrane potential (opened channels). The voltage gated sodium channels could induce such a large depolarization of the membrane, being also consistent with the reliable effect of TTX which blocks the Na channels as illustrated in figure 3b. Although it should be confirmed by controlling the opening and closing of the targeted channels specifically.

The conductance fluctuations could be caused by the ionic current generated during an action potential, which is the highest expected electrical signal. However the duration and the shape of the measured signal are incompatible with action potentials, which imply a fast rising and decaying spike lasting for only a few milliseconds. On the other hand, the shape of the measured signal strongly resembles the fluctuations of single ion channels present in the neuronal membrane. The ion channels exhibit two states, an open and a closed one, and the transition between these two states generates square shaped signals lasting for up to several hundred milliseconds.[35] Thus, considering the suppression of the signal by adding TTX and also after fixing the cells (figure S6), the conductance fluctuations observed in graphene could stem from the random opening and closing of ion channels distributed in the neuronal membrane. Indeed graphene devices of macroscopic dimensions were already shown to be

able to detect weak and nanoscale signals such as the activity of a single artificial ion channel, [36] opening a wide field of investigations for field effect transistors which should further amplify the detection of the ion channels activity.

2.3. The capacitive neuron-FET coupling

As shown in figure 4, RT signals induced by the neurons were observed over a wide range of liquid gate voltages, showing varying amplitude which increased for liquid potential values exceeding V_D. The higher RTS amplitude can be attributed to the increasing net current through the transistor channel, such as the signal amplitude also exhibits a linear dependence on the applied bias voltage V_{SD}, which is proportional to the net drain current (figure S7). More importantly, the polarity inverses from positive to negative conductance peaks once the G-FET is tuned from hole to electron conduction regime which is in agreement with the expected sign inversion due to the change of the polarity of the charge carriers in the transistor channel. This result is crucial as it highlights the field effect origin of the RTS signals which do not result from faradic currents (charge injection only).[8,9] It is typical measurements obtained for all recording with the GFETs (figure S9). Additionally with the increasing liquid potential, we observe (for the small devices only) less and shorter channel closings at highest applied liquid gate potential (V_{LG} = 0.85 V figure 4b). While the exact origin remains unknown, low faradic currents which should increase with the gate voltage might impact the opening frequency of the ion channels. The flattening of the transconductance in the presence of neurons (figure S5) could be an alternative explanation. However, a similar trend should be observed for all the gating values in the electron regime (figure S5) which is clearly not observed (figure 4b for V_G=0.55V). Moreover, the large gating values seem impact rather the occurrence than the amplitude of the response signal regarding the remaining high spikes at the beginning of the trace (inset figure 4b for V_G=0.85V). The depression of the transconductance was observed for GFETs on which we observed RTS (figure S4B), and might rather confirm the presence of tiny contacts with the

cell membrane and the formation of weak links which are indeed required for the detection of small and local potential variations.[37]

3. Discussion

3.1. Contribution of 1D defects for the detection of ion channels

Ion channels exhibit a very local and weak electrical signal (about 10^8 ion per channel per second are involved for fast sodium channel), which first appears unlikely to be detected by a large area graphene FET. The explanation could come from the presence of nanoscale defects which could dominate the transport properties of the total channel width.

Edge states have been shown to play a critical role for the charge carrier transport in graphene nanoribbons, resulting from rough edges, imperfections of the graphene layer or the broken symmetry of the hexagonal lattice and change in bonding. Regarding the unperfected lithographical, etching and transfer techniques, edge states may indeed exist in our GFETs. However their contributions for the detection of ion channels, which should also be the highest for the smallest graphene channel, is not observed certainly because the channel remains large 20µm (figure 2). Also, there are negligible edges defects on the largest GFET (no edges, see figure 2a and S8) and yet the detection has been found to be the most probable.

In another hand, the network of grains boundaries which naturally forms in CVD-grown polycrystalline graphene layers, generates a patch work across the total width of the GFET channels, and provides both the required sensitivity and the contact with the cell for sensing small change of extracellular potential. GBs generate potential barriers, with locally tunable fluctuating transmission properties, through the transistor channel. Due to their one dimensional nature, the transport properties of GBs are extremely sensitive to local environmental changes, such as nanoscale gating by single ion channel. The formation of tunnel (p-p'-p) junctions across the GBs between two single crystalline graphene grains was first demonstrated with several STM studies in CVD grown graphene.[39-41] Then Yasaei et al.[26] have shown that the performance of graphene sensors is not a macroscopic property but is

rather dominated by 1D potential barriers formed by GBs, which offer a strongly increased sensitivity to single molecule adsorption. The sensitivity of polycrystalline graphene appears 4 times more sensitive than single crystalline grain, reaching a maximum value when one GB crosses the entire width of the GFET channel,[25, 26] in agreement with our recordings (figure 5c). In such configuration, the charge carrier current is dominated by the GB conductivity, such that small conductance fluctuations of ion channels could locally trigger the transmission through the GB, resulting in a global resistance fluctuation of the transistor channel. This works based on chemical interaction have been further extended to charge effect. Kochat et al.[38] have demonstrated that the electrical noise arising from GBs is 3000 to 10,000 times larger than the one emitted by single crystalline graphene and have highlighted its potential for sensing applications.

Our devices are also expected to form a 2D random network of weak-links created by the GBs (schematic in figure 5d) whom quantity is controlled by varying the size of the transistor channel (figure 5d). While the mechanism by which neurites tune the GBs transmittance is different from adsorption of chemical species in the gas phase, the electronic transmission through the GB tunnel junctions could explain the highly sensitive near field detection of ion channels that are in close vicinity of the GB, as illustrated in figure 5b. Once the ion channel opens, the ionic current above the grain boundary tunes its energy level to the values matching the Fermi level of neighboring graphene grains, resulting in a higher transmission of the current through the GB and increased conductance of the graphene transistor. Obviously the polarity of the detected signal will depend on the conduction regime of the graphene transistor (the GB and the single grain being gated by the surrounding liquid gate) and the fluctuation amplitude $\Delta G/G$ will increase with decreasing length of the transistor channel, which is in good agreement with our experimental observations (figures 5 and 2). Based on these previous model and regarding the relative conductance modulation which is slightly the same for the hole and electron regime (figures 4 and S9), we can expect a p-p'-p doping

distribution switching from p' to p'' (inversely n-n'-n, switching from n' to n'' in the electron regime). In fact, the reported sensitivity for 2 serial GBs is around 30%,[26] which is similar to the sensitivity of our 40x50µm² GFETs (figure 5) along which we also expect ~2 GBs regarding the size of single grain (figure 1).

3.2. Shape and amplitude of the expected extracellular signals

When the probed area of the membrane decreases (about 1µm² corresponding to ~10 channels), the Markov model based on discrete stochastic ion channel populations predicts that the detected neuronal activity will resemble the activity of a single ion channel[42] with unexpected large amplitude response, confirming our assumption on GBs-assisted detection which provide the required nanoscale contact to the cell. The large extracellular response (mV) generated by the opening and closing of ion channels can be explained using the standard equivalent circuit of the Hodgkin–Huxley model shown in figure 1a. The *DC* voltage response of the membrane (capacitive part is neglected) is function of the conductance of the membrane, the conductance of the ion channels and the ion specific Nernst potential (E_i) such as $\Delta V \sim G_i/(G_i + S_j \times G_m) \times E_i$. However, while the conductance of the membrane is proportional to the probed surface $S \times G_m$ with G_m the membrane conductivity per unit area (~3pS.µm^{-2}), each coupled channel contributes equally for the total conductance $G_i = \sum g_i$ with g_i being independent of the probed area. Therefore, when addressing locally the membrane its conductance becomes negligible and the opening of single or few ion channels can induce an unexpected high variation of the membrane potential, being the highest for sodium channel which have therefore the highest probability to be detected. Obviously, the extracellular voltage is reduced by background ions currents, the distance to the cell and the seal resistance, but it could explain how a nanometer scale ion channel could generate such a high extracellular voltage at the GBs, gate the GBs and affect the transport through the graphene transistor channel.

We can roughly estimate the number of sodium channels n_{NA} expected per neurites/GBs (crossings) matching pair. Considering the density of sodium channel[42] (about 60 channels.μm^{-2}) and the cross section between the neurite and the grain boundary $d_{axon} \times d_{GB}$ (5×0.01 μm^2), we obtain about $n_{NA} \sim 3$ ion channels per GB, with 5µm and 10 nm the average widths of neurites and GBs. [38] The total number of coupled ion channels over the entire transistor is well higher, being proportional to the number of interacting (neurites/GBs) pair and increasing with the graphene channels size. But locally only few ion channels (~3) are sensed by the GB giving rise to step like signals instead of spikes.[42] The coincidently opening of the few active ion channels could explain the occurrence of intermediate states in the most sensitive devices (figure 4). For larger devices, we rather observe a widening of the two-state histogram (2-3 times wider) resulting from a higher dispersion of the GFETs responses. The neurites/GBs matching pairs do not interact equally (because of different coupling, different GBs electronics properties, and different coupled area of the neuron) and thus their contributions are expected to be slightly different especially when increasing the size of graphene channel (or number of GBs) which also reduces the device sensitivity (figure 5c) and could prevent the resolution of discrete excited states.

3.3. The grain boundaries model

The probability to observe RTS decreases when reducing the transistor channel area, as illustrated in figure 5d. While RT signal was frequently observed on large graphene transistors, it was never measured on the smallest devices. This observation can also be explained within the GB-hypothesis. The typical spacing λ between GBs is around 30-40 µm (at least below 50 µm) with our pulsed growth process, as shown in figures 1c-d and 5d. Supposing that one GB is still present on the GFET it should be properly aligned (perpendicular to the width) in order to cross all the width of the transistor channel, otherwise mono-crystalline pathways bypass the GB and the required sensitivity and spatial resolution for detecting the ion channel are lost (see figure S10). Consequently the probability of having

one grain boundary crossing the entire width of short devices ($L<\lambda$) and at the same time matching the ion channel position in near field is quite low and could explain the fact that we never observed RTS on smallest G-FETs with a channel size of 20×10 μm² even with higher neurons density (at least on the 40 devices tested, several cultures, seeding density ranging from 50 to 150kc/ml). On the other hand, GBs network naturally forms on larger graphene channels, thus there is no more (mono-crystalline) parallel channel through a single grain (figure S10B), which increasing the probability to have a matching pair of a fluctuating ion channel and a grain boundary, and thus the probability of observing RT signals originating from neuronal activity. Indeed, this probability P to interact with a single ion channel is proportional to the number of ion channels/grain boundaries matching pairs N_i which is proportional to the number of neurites crossing a grain boundary (W/ω, with ω the effective neurites spacing) multiplied by the number of GBs (L/λ) as illustrated with the schema figure 5d and in agreement with our results. In another hand, the probability of matching an *IC/GB* pair leading to ion detection is almost $P \sim 0$ when the length of the graphene channel becomes smaller than the single grains diameter ($L<\lambda$), independently of the number of neurites and ion channels which is in agreement also with the observed detection threshold set by the sensors length (L_{th}~20μm) in this experiment.

3.4. The detection efficiency

From the dependence of the RTS observation probability P with the device size (figure 5d), we found that the detection efficiency (P/N_i) for the several devices remains low, increasing slightly when reducing the device size (around 0.1%, 0.6%, 2%). Given the high density of grain boundaries in CVD graphene, an important question is why we observe only the contribution of a few ion channels. Here we can identify several reasons which might be responsible for this strongly localized detection. Despite the high amount of grain boundaries in the large area devices, the GBs exhibit a strong variation of their electronic properties,[38,42]

such that not every GB contributes to the same extend to the transport through the graphene channel. Also the low seeding density of neurons used in our experiments results in a low covering fraction of the underlying graphene (ca. 15-20%) and thus lowers the probability to obtain a matching GB/ion channel. Additionally, the adhesion of the neuronal membrane to the substrate (especially along the neurites) is not homogeneous, but rather exhibits infrequent anchor spots strongly coupled to the substrate.[43,44] Thus the membrane might be mostly insufficiently coupled to the device preventing the occurrence of a RT signal.

While specific and controlled molecular adsorptions were used to model the positive impact of grain boundaries on the GFETs sensitivity,[26] our sensing experiments are performed in liquid environment and thus differ from adsorption of chemical species in the gas phase. In liquid experiment, a cleft (a liquid junction) forms between the neurons and the grain boundaries. Both the cleft thickness and the resistance through the bath are of primary importance for the near field detection of ions channels. This interface was deeply characterized, and transmission electron micrographies[46] revealed that polylysine coating offers the closest contact to the cell (thinnest interface d~35-40nm) compared to other adhesive proteins, allowing the formation of focal adhesion points where membrane areas are even closer to the substrate d≤10nm. Because, the adhesion is crucial for the survival, the neuritogenesis and the maturation of fragile primary hippocampal neurons, we can assume that strong contacts occur also between the neurons membrane and the PLL coated graphene, at least similar to the ones reported for HEK cell on silicon oxide substrate. Since few years graphene has appeared to promote the growth of numerous cells in culture, being more adhesive than the conventional glass or silicon oxide substrates for neurons[11,47] and stem cells[48] also. While the microscopic mechanisms which sustain such a high neuronal affinity are still under investigations, strong non-covalent interactions have been observed when interfacing graphene with polylysine. The hybrid PLL-Graphene substrate which is further positively-doped (than the pristine graphene) could increase the electrostatic interactions with

the negatively charged neurons membrane and might support the formation of close contacts to the cell membrane, providing the required strong coupling for ions channels detection. Similar improvement of neuronal adhesion on carbon nanotubes has already been suggested to favor electrical shortcuts by forming tight contacts with the cell membranes. [49] Therefore, based on these frameworks, we expect similar nanometer-thick contacts on graphene, which can explain how such small currents through ion channels can be sensed while operating in liquid media and further amplified by the obvious existence of GB along our GFETs. The detection efficiency is indeed expected to be reduced in comparison with the Kochat et al and Yasaei et al studies, being also dependent on the density of the focal adhesion points which covers a fraction (10-15%) of the membrane only. [43,44,46]

In perspective to this work, we aim to investigate further the ICs/GBs coupling and the near field detection mechanisms. One interesting strategy would be to isolate few ion channels above one single grain boundary that can be previously characterized in term of transport properties. This could be obtained in two steps: (1) by controlling the position of grain boundaries over the substrate and (2) by aligning a defined number of neurites along the 1D-junction created by the grain boundary, with micro-patterning or microfluidic techniques. Such studies would provide new way to sense the activity of ion channels with integrated sensors, offering the ability to interface simultaneously a large amount of neural cells.

4. Conclusion

In summary, we provide strong evidence that we can detect the spontaneous activity of single ion channels in neural cells in-situ grown on macroscopic polycrystalline graphene FETs. We attribute the sensing to highly sensitive grain boundaries randomly distributed in CVD graphene. We demonstrated a nanoscale and time stable detection of the activity of a single ion channel sensitive to drug injection. In this sense, GB-based sensors offer a new promising platform for monitoring fundamental electrophysiological processes in living cells with nanoscale resolution. We envision the possibility to control the geometry of grain

boundaries network to map the single ion channel activity over a large population of neurons with high spatial and temporal resolution using highly neuro-compatible materials.

Experimental Section

CVD graphene growth and transfer onto arbitrary substrates. High-quality monolayer graphene was grown on copper foil (25μm thick, 99.8% purity, Alfa-Aesar) using pulsed chemical vapor deposition (CVD) as reported earlier. [29] Pulses of CH_4 (2 sccm 10s, then 60s off) are injected into the growth chamber with hydrogen atmosphere. Continuous CH_4 flow usually results in an increasing amount of carbon atoms dissolved in Cu foil defects. The following segregation of carbon atoms to the surface of the Cu foil leads to an uncontrolled formation of graphene multilayers. In contrast, using pulsed CH_4 flow the copper foil is periodically exposed to pure hydrogen, which binds the segregated/dissolved carbon atoms and carries them out from the growth chamber, preventing the development of multilayer patches. Before the growth, Cu foil is cleaned in acetone and annealed in diluted H_2 atmosphere (dilution in Ar at 10%) at 1000°C for 2h. Pieces of Cu foil of about 4×4 mm² with graphene layer grown on top are covered with PMMA on the graphene side and then wet etched in ammonium persulfate solution (0.1 g/ml, 2h at room temperature). After complete etching of Cu, graphene-PMMA stack is rinsed in 6 subsequent deionized (DI) water baths to remove the residual etchant. Then the graphene-PMMA film floating on the DI water surface is scooped from below onto a clean substrate and dried at room temperature. Finally PMMA is removed in an overnight acetone bath followed by a 3 h long thermal annealing at 300°C in vacuum.

Device fabrication. High quality monolayer graphene was transferred on sapphire and silicon on insulator SOI and glass substrates with predefined alignment marks. Some graphene sheets were directly contacted by Ti/Au leads using standard photolithography. On the other samples, graphene was patterned into smaller channels using photoresist masks and

etched by oxygen plasma (figure 2a). Source-drain contacts were defined by a second optical lithography step followed by the metallization and resist lift-off. Finally, a SU8 resist pattern was used to electrically insulate the metallic contacts from the ionic solution. Using this fabrication protocol, arrays of graphene transistors with graphene channel dimensions of W×L = 1000×250 μm², 40×250 μm², 40×50 μm² and 20×10 μm² were realized, where W is the channel width and L the length.

Cell culture and immunofluorescence imaging. Primary hippocampal neurons were dissociated from E16.5 mouse embryos and seeded with a density of $0.5 \cdot 10^5$ cells/cm² onto sterilized poly-L-lysine coated chip surface following previously reported culturing protocol.[11] A PDMS chamber (200-300μl) is fixed on the chip for containing the cells and mediums, while keeping dried the deported contacts. The seeded neurons were incubated at 37°C and 5% CO_2 in the attachment medium (MEM supplemented with foetal bovin serum) and replaced 3 to 4 hours later by glial conditioned Neurobasal medium supplemented with AraC (1 μM) to stop proliferation of glial cells. Medium was changed once a week. Presence of cells above the device is checked before the measurement with a reflection microscope (Olympus BX51) for silica substrate. On the sapphire substrate, the neurons growth is observed all along the culture with conventional transmission microscope providing better resolution of the neurites position above the device. After recordings, immunofluorescence staining was performed to locate the cells above the devices and characterize their maturation stage. Neurons were fixed in 4 % paraformaldehyde (10 min) and immunostained with Phalloidin, DAPI and anti-synapsin primary antibody to visualize the actin filaments, nucleus and pre-synaptic vesicles respectively.

Transistor characteristics and cell activity recordings. The GFETs sensitivity is characterized by applying a DC liquid front gate voltage V_{LG} in the cell culture saline medium surrounding the devices through a quasi-reference Pt-electrode. Electronics properties of the devices are measured with a shielded probe station in controlled atmosphere with 5% of CO_2.

The drain and gate electrodes are voltage biased and the drain source current is amplified and filtered for recording. Low pass filters prevent incoming noise from contact lines to the device and the medium. Analog out and inputs are interfaced with a FPGA card. Before cell recording, V_{DS} and V_G are chosen to reach the maximum sensitivity in the hole regime by measuring the I_{SD} -V_G curves. Before the culture, the sensitivity of G-FETs is also obtained by applying a DC liquid front gate voltage V_{LG} in the cell culture saline medium surrounding the devices through a quasi-reference Pt-electrode.

Acknowledgements
The authors thank G.Bres, J.L. Moncellin for the excellent electronics support, Z. Han, L. Marty and N. Bendiab for the background work on the graphene growth and characterization, G. Cunge and D.Ferrah from the LTM for the specific GBs etching treatment. The authors gratefully acknowledge financial support from the University Joseph Fourrier (SMINGUE project), from la Région Rhône-Alpes (COOPERA project), and from the french Agence Nationale de la Recherche under the projects ANR-10-LABX-51-01 (Labex LANEF du Programme d'Investissements d'Avenir) the Lab Alliances on Nanosciences - Energies for the Future.

References

1. Obien, M. E. J.; Deligkaris, K.; Bullmann, T.; Bakkum, D. J.; Frey, U. *Front. Neurosci.* 2015, 8, 423.

2. Lambacher, A.; Jenkner, M.; Merz, M.; Eversmann, B.; Kaul, R. A.; Hofmann, F.; Thewes, R.; Fromherz, P. *Appl. Phys. A* **2004,** 79, 1607-1611.

3. Fromherz, P. In: Nanoelectronics and Information Technology, Vol. 2 (Eds: R. Wasser), Wiley-VCH Verlag, Berlin, Germany (2003).

4. Patolsky, F.; Timko, B. P.; Yu, G.; Fang, Y.; Greytak, A. B.; Zheng, G.; Lieber, C. M. *Science* **2006,** 313, 1100-1104.

5. Polikov, V. S.; Tresco, P.A.; Reichert, W.M. *Jnal Neuro. Meth.* **2005,** 148, 1-18.

6. Marin, C.; Fernandez, E. *Front Neuroeng.* **2010,** 3(8),

7. Kostarelos, K.; Novoselov, K. S. *Nat. Nanotechnol.* **2014,** 9, 744.

8. Hess, L. H.; Jansen, M.; Maybeck, V.; Hauf, M. V.; Seifert, M.; Stutzmann, M.; Sharp, D.; Offenhäusser, A.; Garrido, J. A. *Adv. Mater.* **2011,** 23, 5045-5049.

9. Cohen-Karni, T.; Qing, Q.; Li, Q.; Fang, Y.; Lieber, C. M. *Nano Lett.* **2010,** 10, 1098-1102.

10. Uesugi, E.; Goto, H.; Eguchi, R.; Fujiwara, A.; Kubozono, Y. *Sci. Rep.* **2013,** 3, 1595.

11. Veliev, F.; Briançon-Marjollet, A.; Bouchiat, V.; Delacour, C. *Biomaterials* **2016,** 86, 33-41.

12. Schwierz, F. *Nat. Nanotechnol.* **2010,** 5, 487-496.

13. Katsnelson, M. I.; Fasolino A. *Acc. Chem. Res.* **2012,** 46, 97.

14. Titov, A.;V., Kral, P.; Pearson, R. *ACS Nano* **2010,** 4, 229.

15. Fabbro, A.; Scaini, D.; Leon, V.; Vázquez, E.; Cellot, G.; Privitera, G.;Lombardi, L.; Torrisi, F.; Tomarchio, F.; Bonaccorso, F.; Bosi, S.; Ferrari, A.C. *ACS Nano* **2015,** 10(1), 615-623.

16. Bendali, A.; Hess, L. H.; Seifert, M.; Forster, V.; Stephan, A. F.; Garrido, J. A.; Picaud, S. *Adv. Healthc. Mater.* **2013,** 2, 929-933.

17. Lorenzoni, M.; Brandi, F.; Dante, S.; Giugni, A.; Torre, B. *Sci. Rep.* **2013,** 3, 1954.

18. Park, S. Y.; Park, J.; Sim, S. H.; Sung, M. G.; Kim, K. S.; Hong, B. H.; Hong, S. *Adv. Mater.* **2010,** 23, 263.

19. Tang, M.; Song, Q.; Li, N.; Jiang, Z.; Huang, R.; Cheng, G. *Biomaterials* **2013**, 34, 6402-6411.

20. Chen, C. H.; Lin, C. T.; Hsu, W. L.; Chang, Y. C.; Yeh, S. R.; Li, L. J.; Yao, D. J. *Nanomedicine : Nanotechnology, Biology and Medicine* **2013,** 9(5), 600-604.

21. Mattei, T. A.; Rehman, A. A. *Neurosurgery* **2014,** 74 (5), 499-516.

22. Li, X.; Cai, W.; An, J.; Kim, S.; Nah, J.; Yang, D.; Piner, R.; Velamakanni, A.; Jung, I.; Tutuc, E.; Banerjee, S. K.; Colombo, L.; Ruoff, R. S. *Science* **2009,** 324, 1312–1314.

23. Huang, P. Y.; Ruiz-Vargas, C. S.; van der Zande, A. M.; Whitney, W. S.; Levendorf, M. P.; Kevek, J. W.; Garg, S.; Alden, J. S.; Hustedt, C. J.; Zhu, Y.; Park, J.; McEuen, P. L.; Muller, D. A. *Nature* **2011,** 469(7330), 389-392.

24. Yu, Q.; Jauregui, L. A.; Wu, W.; Colby, R.; Tian, J.; Su, Z.; Cao, H.; Liu, Z.; Pandey, D.; Wei, D.; Chung, T. F.; Peng, P.; Guisinger, N. P.; Stach, E. A.; Bao, J.; Pei, S-S.; Chen, Y. P. *Nat. Mater.* **2011,** 10(6), 443-449.

25. Salehi-Khojin, A.; Estrada, D.; Lin, K. Y.; Bae, M-H.; Xiong, F.; Pop, E.; Masel, R. I. *Adv. Mater.* **2012,** 24, 53-57.

26. Yasaei, P.; Kumar, B.; Hantehzadeh, R.; Kayyalha, M.; Beskin, A.; Repnin, N.;Wang, C., Klie, R. F.; Chen, Y. P.; Kral, P.; Salehi-Khojin, A. *Nat. Commun.* 2014, 5, 4911.

27. Fromherz, P. *Chem. Phys. Chem.* **2002,** 3, 276-284.

28. Graf, D.; Molitor, F.; Ensslin, K.; Stampfer, C.; Jungen, A.; Hierold, C.; Wirtz, L. *Nano Lett.* **2007,** 7, 238-242.

29. Han, Z.; Kimouche, A.; Kalita, D.; Allain, A.; Arjmandi-Tash, H.; Reserbat-Plantey, A.; Marty, L.; Pairis, S.; Reita, V.; Bendiab, N.; Coraux, J.; Bouchiat, V. *Adv. Funct. Mater.* **2014,** 24, 964-970.

30. Fletcher, T. L.; Cameron, P.; De Camilli, P.; Banker, G. *J. Neurosci.* **1991,** 11(6), 1617-1626.

31. Kirton, M. J.; Uren, M. J. *Adv. Phys.* **1989,** 38, 367–468.

32. Clément, N.; Nishiguchi, K.; Fujiwara, A.; Vuillaume, D. *Nat. Commun.* **2010,** 1, 92.

33. Li, J.; Pud, S., Petrychuk, M.; Offenhausser, A.; Vitusevich, S. *Nano Lett.* **2014,** 14(6), 3504-3509.

34. Sharf, T.; Wang, N. P.; Kevek, J. W.; Brown, M. A.; Wilson, H.; Heinze, S.; Minot, E. D. *Nano Lett.* **2014,** 14(9), 4925-4930.

35. Magistretti, J.; Ragsdale, D. S.; Alonso, A. *J. Neurosci.* 1999, 19(17), 7334-7341.

36. Wang, Y. Y.; Pham, T. D.; Zand, K.; Li, J.; Burke, P. J. *ACS Nano* **2014,** 8(5), 4228-4238.

37. Kumar, B.; Min, K.; Bashirzadeh, M.; Farimani, A. B.; Bae, M. H.; Estrada, D.; Kim,Y. D.; Yasaei, P.; Park, Y. D.; Pop, E.; Aluru,N.R.; Salehi-Khojin, A. *Nano Lett.* **2013,** 13(5), 1962-1968.

38. Kochat, V.; Tiwary, C. S.; Biswas, T.; Ramalingam, G.; Hsieh, K.; Chattopadhyay, K.; Raghavan, S.; Jain, W.; Ghosh, A. *Nano Lett.* **2015,** 16(1), 562-567.

39. Koepke, J. C.; Wood, J. D.; Estrada, D.; Ong, Z. Y.; He, K. T.; Pop, E.; Lyding, J. W. *ACS Nano* **2013,** 7(1), 75-86.

40. Nemes-Incze, P.; Yoo, K. J.; Tapasztó, L.; Dobrik, G.; Lábár, J.; Horváth, Z. E.; Hwang, C.; Biró, L. P. *Applied Physics Letters* **2011**, 99(2), 023104.

41. Clark, K. W.; Zhang, X. G.; Vlassiouk, I. V.; He, G.; Feenstra, R. M.; Li, A. P. *ACS Nano* **2013**, 7(9), 7956-7966.

42. Strassberg, A. F.; DeFelice, L. *J. Neural Comput.* **1993,** 5(6), 843-855.

43. Bernal, R.; Pullarkat, P. A.; Melo, F. *Phys. Rev. Lett.* **2007**, 99(1), 018301.

44. O'Toole, M.; Lamoureux, P.; Miller, K. E. *Biophys. J.* **2008**, 94(7), 2610-2620.

45. Yang, K.; Li, Y.; Tan, X.; Peng, R.; Liu, Z. *Small* **2013,** 9 (9-10), 1492-1503.

46. Wrobel, G.; Höller, M.; Ingebrandt, S.; Dieluweit, S.; Sommerhage, F.; Bochem, H. P.; Offenhäusser, A. *Journal of The Royal Society Interface* **2008,** 5(19), 213-222.

47. Li, N.; Zhang, X.; Song, Q.; Su, R.; Zhang, Q.; Kong, T. ; Liu, L.; Jin, G. ; Tang, M.; Cheng, G. *Biomaterials* **2011,** 32(35), 9374-9382.

48. Park, S. Y.; Park, J.; Sim, S. H.; Sung, M. G.; Kim, K. S.; Hong, B. H.; Hong, S. *Advanced Materials* **2011** 23(36).

49. Cellot, G.; Cilia, E.; Cipollone, S.; Rancic, V.; Sucapane, A.; Giordani, S.; Gambazzi, L.; Markram, H.; Grandolfo, M.; Scaini, D.; Gelain, F.; Casalis, L.; Prato, M.; Giugliano, M.; Ballerini, L. *Nature nanotechnology* **2009** 4(2), 126-133.

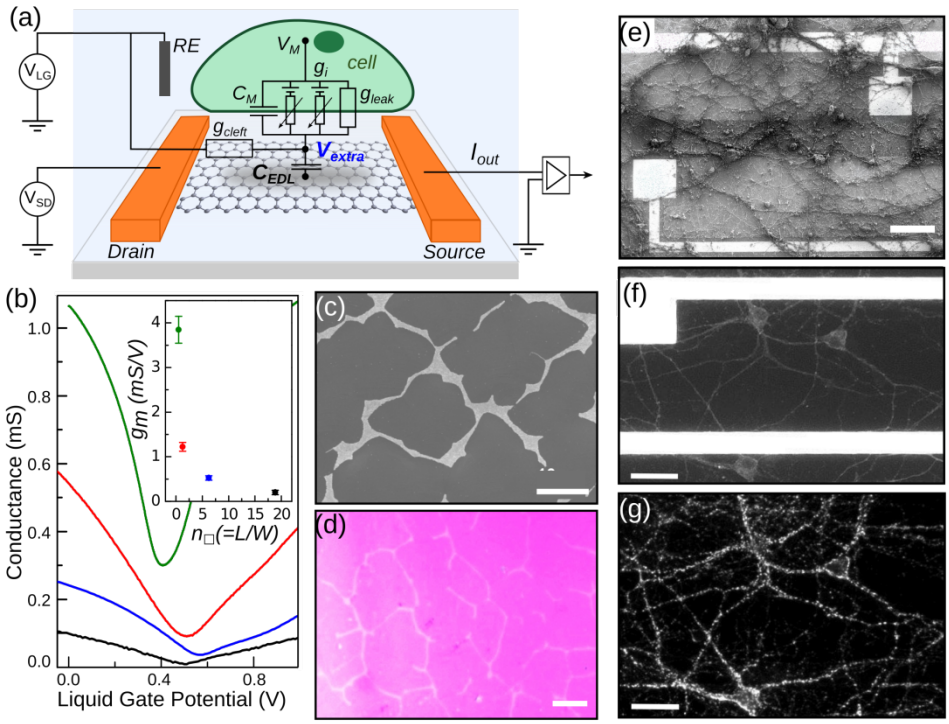

Figure 1. (a) Equivalent electrical circuit of cell-FET hybrid system: V_{SD}, V_{LG} and V_{extra} are the bias source-drain voltage, the liquid gate potential, and the extracellular potential in the cleft generated by the electrical activity of the cell. V_{LG} is set using a reference electrode RE. C_{EDL} is the capacitance of the electric double-layer (EDL) formed at the graphene/liquid interface and g_{cleft} is the seal conductance between the cleft and the bath. Trans-membrane ionic currents are modeled with the Hodgkin-Huxley elements: a parallel membrane capacitance C_M and leak conductance g_{leak} and the conductance g_i of voltage gated ion channels modulated by the membrane potential V_M. The local potential change V_{extra} triggered be the cell results in the modulation of the measured output current I_{out}. (b) Conductance vs. liquid gate potential curves for G-FETs with different width-to-length ratios of the transistor channel: $W \times L$=20×10 µm² (green line), 40×50 µm² (red line), 40×250 µm² (blue line) and 40×750 µm² (black line). The inset illustrates the non-linear dependence of the normalized transconductance of G-FETs with the number of square (L/W ratio). Representative scanning electron (c) and optical (d) micrographs of a typical CVD grown graphene, for which the growth is stopped shortly before the complete coalescence of single graphene grains (darkest area), showing the expected GBs network (brightness lines). Scale bars are 15µm (e) Representative scanning electron micrograph of 21 days old hippocampal neurons interfaced with the G-FETs. The 250 µm-long graphene strip appears darker between the two bright metallic electrodes. Representative optical images of the neurons stained with YL1/2 (f) and synapsin (g) for labeling the microtubules and the synapses. Scale bars are 50 µm.

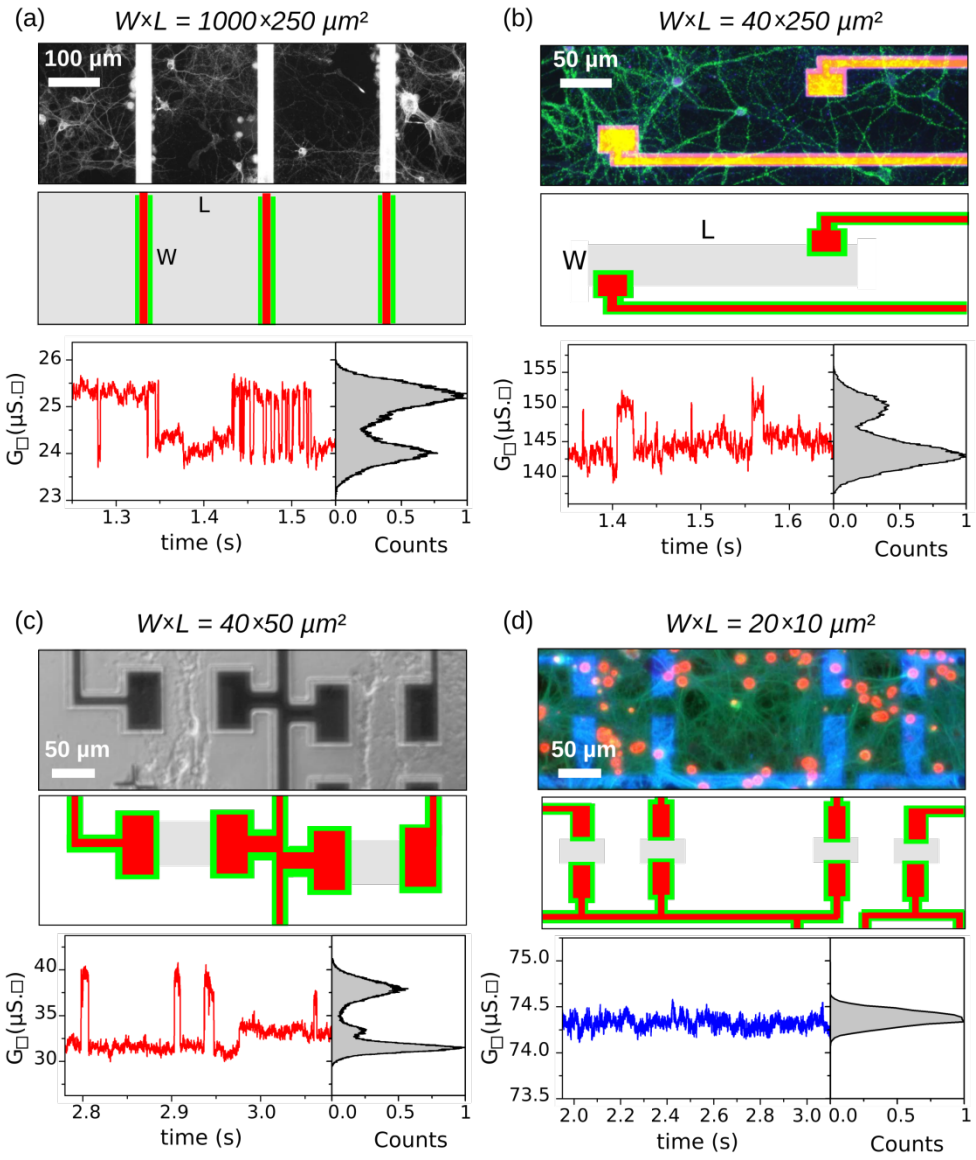

Figure 2. Immunofluorescence (a, b, d) and optical (c) micrographs of neurons cultured on graphene FET arrays with different channel dimensions with the corresponding layout and typical square conductivity time-traces and histograms: (a) W×L= 1000×250 µm² (V_{SD} = 50 mV, V_{LG} = 0.2 V), (b) W×L = 40×250 µm² (V_{SD} = 30 mV, V_{LG} = 0.15 V), (c) W×L = 40×50 µm² (V_{SD} = 30 mV, V_{LG} = 0 V) and (d) W×L = 20×10 µm² (V_{SD} = 70 mV, V_{LG} = 0.3 V). In the devices layout, the exposed graphene channel is pictured in grey, the metallic contact lines in red and the isolating resist overlapping and surrounding the electrodes (external part in green). For immunofluorescence, the neurons are stained with synapsin (grey/green) and Dapi (blue/red).

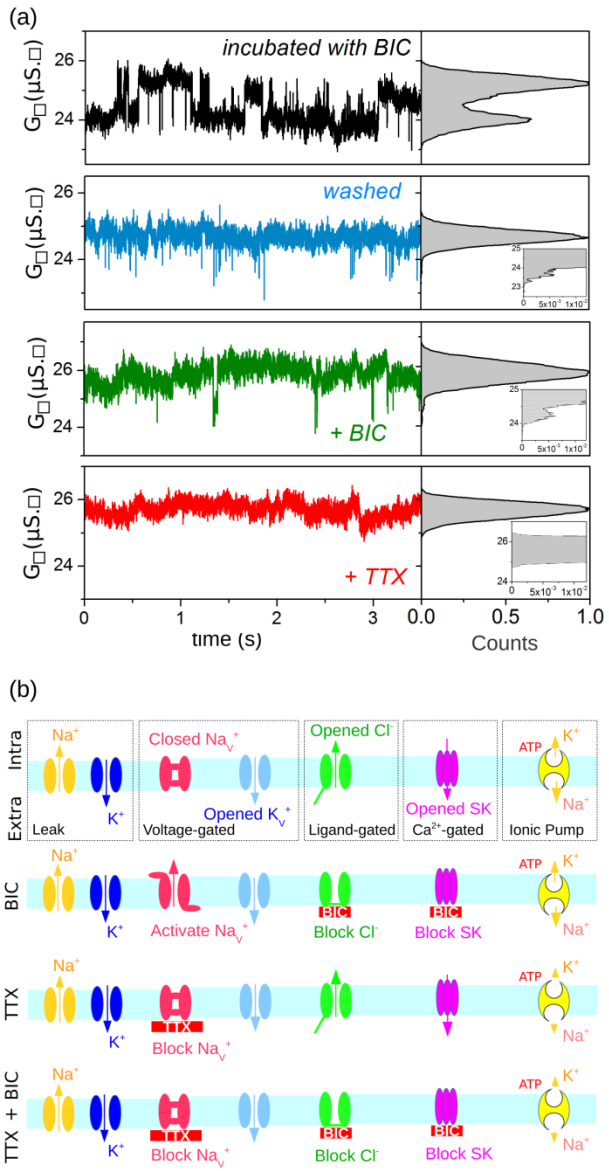

Figure 3. Subsequent square conductivity time traces and corresponding histograms recorded on the same G-FET (W×L = 1000×250 μm²) interfaced to the neurons (V_{SD} = 50 mV, V_{LG} = 0 V). The cell culture medium was first incubated with bicuculline (BIC, black trace), then replaced by fresh medium (washed, blue trace), once again supplemented with bicuculline (BIC, green trace) and finally tetrodotoxin (TTX, red trace) was added to the medium. The arrows indicate the emerging of stable two-state conductance behavior once BIC is added. The bottom insets show the zoomed view at the position of the second peak of the current histogram, which corresponds to the excited state. b) Schematic diagram illustrating the expected impact of BIC and TTX on the activity of ion channels. From left to right : sodium (Na^+) and potassium (K^+) leak and voltage-gated channels, ligand-gated chloride Cl^- channels, small conductance calcium activated potassium channels (SK) and the ion pump.

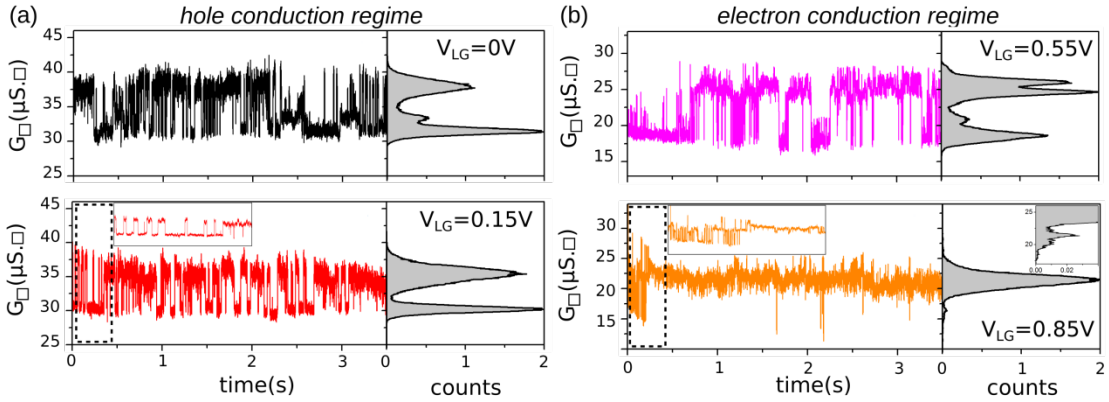

Figure 4. Detection of the activity of ion channels using a 40×50 µm² G-FET. The bias voltage is kept constant at V_{SD} = 30 mV and the potential V_{LG} of the extracellular solution is varied through a Pt-electrode inserted into the cell culture medium. Square conductivity time traces and corresponding histograms recorded in the hole (a) and electron (b) operation regime of the G-FET. A zoomed view of the recorded traces is exemplarily demonstrated for the hole and electron operation regimes at V_{LG} = 0.15V and 0.85V respectively. Enlarged histogram (inset) illustrates the residual activity at V_{LG} = 0.85V.

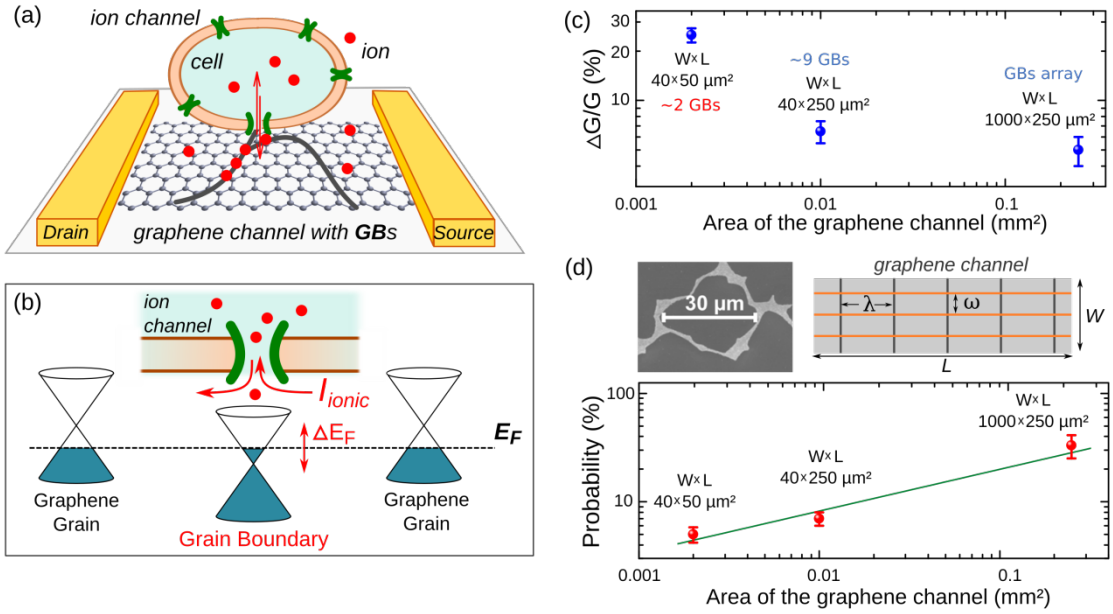

Figure 5. (a) Schematic illustration of a randomly opening and closing ion channel above a graphene grain boundary crossing the transistor channel. (b) Schematic representation of a p-n-p junction formed across the graphene grain boundary. Ionic currents flowing through the ion channel tune the Fermi level of the grain boundary, resulting in varying transmission properties. (c) Dependence of the amplitude of the recorded RTS on the dimensions of the graphene transistor channel. The expected number of GBs along the GFET channels (L/λ) is indicated for each tested design, with λ the size of single graphene grain previously characterized in figure 1c-d. (d) Probability to observe RTS as function of the area of the graphene transistor channel. The image above shows a scanning electron micrograph of a typical CVD growth of continuous graphene sheets (on Cu foil) stopped shortly before the complete coalescence of single graphene grains. The schematic illustrates a simple model of overlapping GBs with spacing λ and ion channels with spacing ω. The observation probability was obtained using several independent cultures and G-FET arrays with identical culturing and sample fabrication protocols. For W×L = 1000×250 µm² - 5 devices out of 15 tested exhibited RTS when interfaced to neurons (2 cultures), for W×L = 250×40 µm² – 2 out of 28 tested devices (1 culture), for W×L = 50×40 µm² - 2 out of ca. 40 tested devices (2 cultures), and for W×L = 20×10 µm² – 0 out of ca. 40 tested devices (2 cultures).

Supporting Information

Sensing ion channels in neuronal networks with graphene transistors

*Farida Veliev, Dipankar Kalita, Antoine Bourrier, Tiphaine Belloir, Anne Briançon-Marjollet, Mireille Albrieux, Vincent Bouchiat and Cécile Delacour**

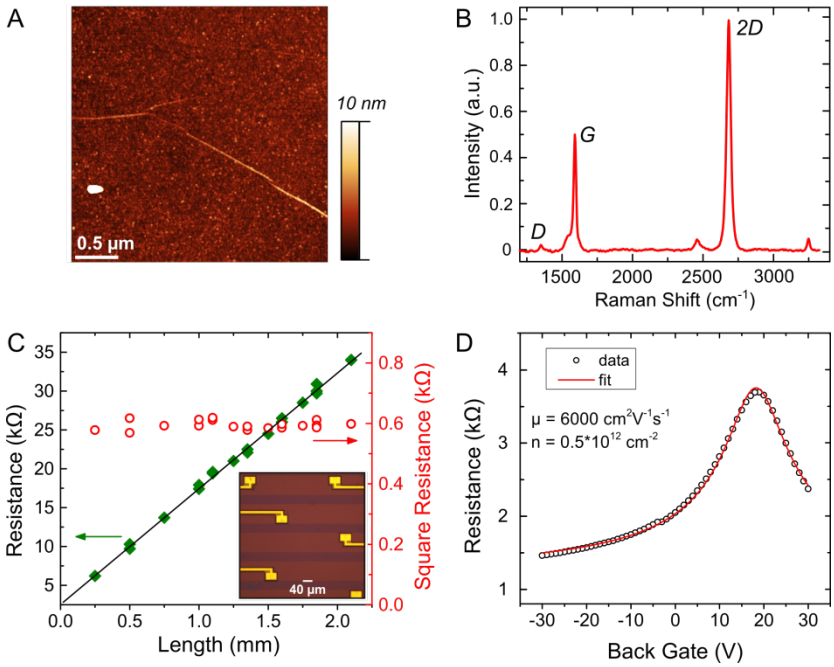

Figure S1. Characterization of graphene sheets after the fabrication of the G-FETs. (A) AFM image of the transistor channel. (B) Raman spectrum of the graphene channel with the characteristic peaks (λ_{exc}=532nm). (C) Determination of the square resistance of graphene using 40 µm wide graphene stripes with varying length *L*. (D) Field effect curve measured on a 40×60 µm² G-FET in ambient environment. The conductance is modulated by a p-doped Si back-gate with 285 nm thick SiO_2 gate oxide. Data (dots) are plotted as resistance vs. back-gate voltage and fitted to extract the carrier mobility μ.

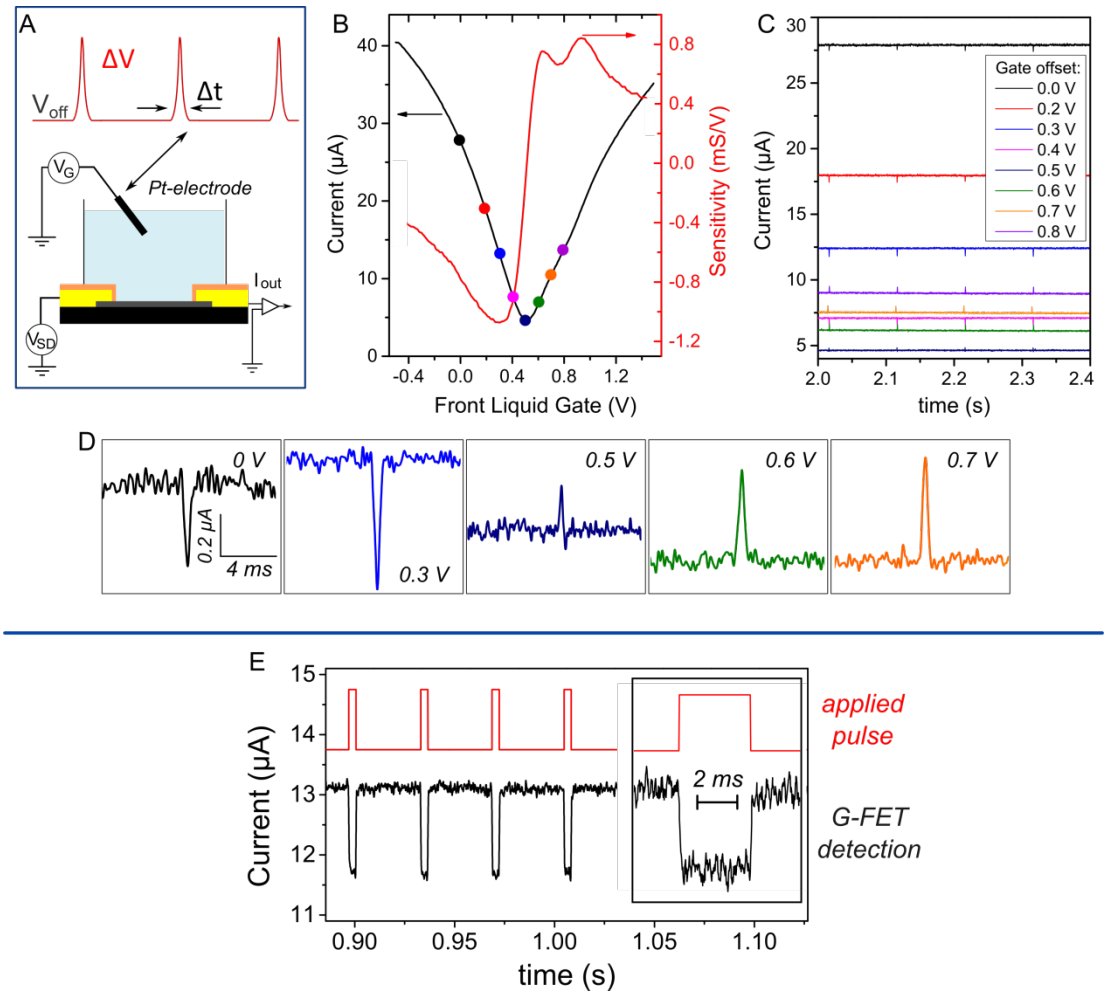

Figure S2. Detection of potential pulses using solution gated G-FETs.(A) Schematic of the experimental setup. Potential pulses with an amplitude ΔV and duration Δt are applied to the liquid gate (culture medium) and the current through the transistor channel is recorded at a constant bias voltage V_{SD}. The gate voltage offset V_{off} sets hereby the transistor working point and thus the sensitivity. (B) Current response and corresponding sensitivity as function of the liquid gate voltage (V_{SD} = 50 mV). (C) Detection of 10mV high and 1ms long potential pulses at different gate offset (indicated with the colored dots in B) (D) Zoom of the pulse responses in the hole regime (<0.5V), around the Dirac point (0.5V) and in the electron regime (>0.5V). (E) G-FET response (black line) to square shaped potential pulses (red line) with ΔV=10mV and Δt=5ms, showing the response time (less than 0.5 ms) to the applied signal.

Patch clamp recordings of spontaneous electrical activity and calcium signaling in cultured hippocampal neurons. Cell attached voltage-clamp technique was used to assess the spontaneous electrical activity at the soma of cultured hippocampal neurons at DIV 21. Figure S3 A shows a typical recording trace. The shape, amplitude and duration of the detected current peaks can be clearly attributed to Na^+ inward currents through the cell. Additionally, calcium imaging was performed to assess the ionics activities along and between the surrounding neurites. After 21 days of culture, 2-5 µl of Fluo-4 AM was added to the cell culture medium depending on the neuron density and incubated for 15 - 60 mins. Then the cell culture medium was changed to remove the excess Fluo-4 AM molecules, and after a short incubation, the neurons were excited by λ_{exc} = 488 nm laser light, and the emission at the wavelength λ_{em} = 515 ± 15 nm was detected. The data were acquired at 4.76Hz using a confocal microscope and commercial software EZ2000 (Nikon). Figures S3 B,C show the recordings of spontaneous calcium signals. The signal propagates from the dendrite to soma and exhibits the expected shape and duration.

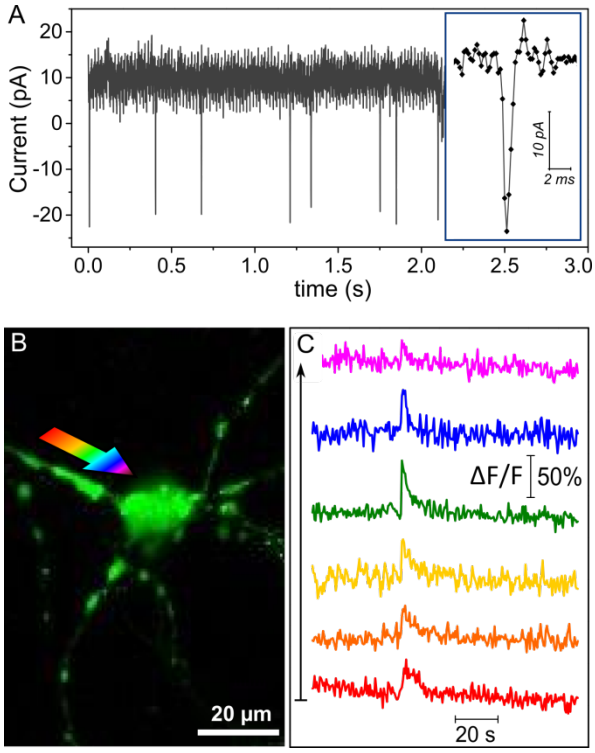

Figure S3. (A) Patch clamp recording on the soma of 21DIV hippocampal neurons with a zoomed current peak. (B) Image of a 21 DIV neuron loaded with calcium sensitive fluorescent molecules (Fluo-4). The arrow represents the patch along which the intensity change of the calcium signal was measured (from black to yellow traces respectively). (C) Recording of calcium signals along the path indicated in B. The detected peaks correspond to an increase in the intracellular Ca^{2+} ion concentration. The neurons were cultured on PLL-coated glass coverslips.

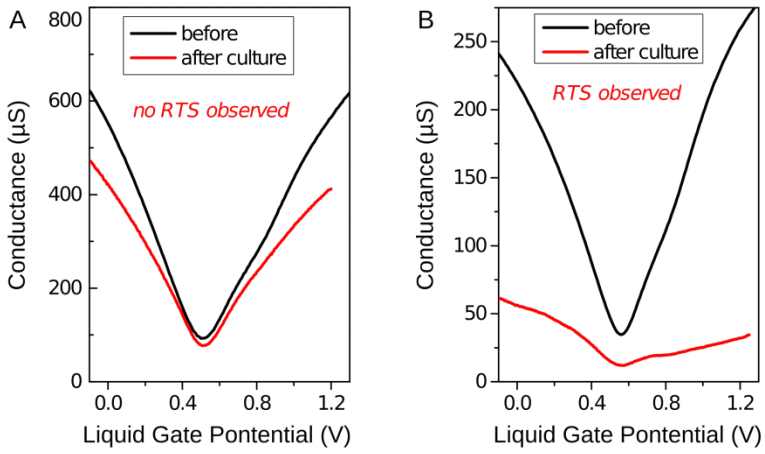

Figure S4. Responses of G-FETs with (A) and without (B) RTS signature of a single ion channel activity measured before (black line) and after (red line) 19 days of neuronal culture. The conductance vs. liquid gate potential $G(V_G)$ is measured (A) on a 40×50 µm² G-FET (V_{SD} = 30 mV). No RTS was observed on this device and the conductance decreased only slightly. (B) $G(V_G)$ measured on a 40×250 µm² G-FET. The drastic decrease of the conductance is representative for all devices, which exhibited RTS. The same behavior is observed on the smallest devices (FIG.S5).

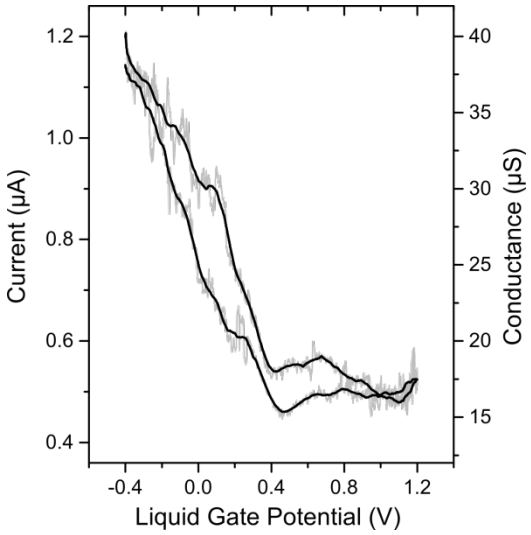

Figure S5. Liquid gate effect on 40×50 µm² G-FET measured before recording the current traces with RTS signature of single ion channel activity. Conductance vs. liquid gate potential measured after 19 days of neuron culture (V_{SD} = 30 mV). Grey line represents the unfiltered signal. The curve was measured prior to recording of current traces with RTS signature of a single ion channel activity. Conductance is tuned by the liquid gate potential from hole to electron conduction regime with the charge neutrality point around 0.45-0.5 V. Notice that the conductance is drastically decreased compared to the devices of the same geometry with no RTS (Fig. S4.A).

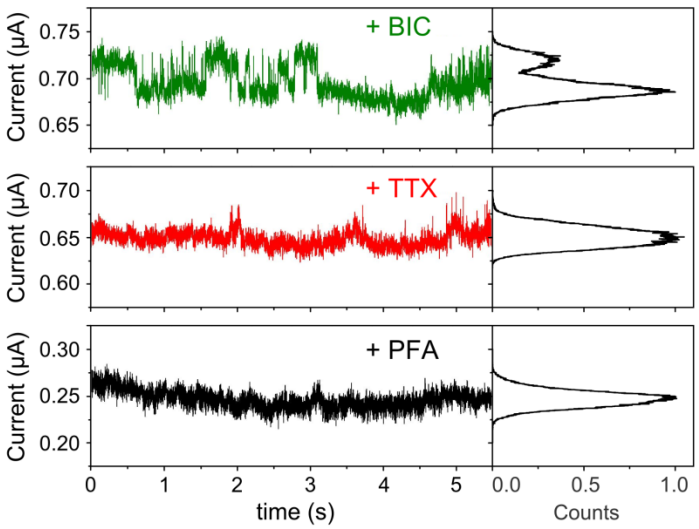

Figure S6. Suppression of RTS by adding tetrodotoxin (TTX) to the extracellular medium. Current traces (left) and corresponding histograms (right) obtained using a 40×250 µm² G-FET interfaced to cultured neurons (DIV19). The current traces are subsequently recorded at a constant bias voltage V_{SD} = 50 mV and liquid gate potential V_G = 0.15 V. Clear two-state conduction fluctuations (RTS) are observed when the cell culture medium is supplemented with bicuculline (BIC, top panel, green trace). The addition of tetrodotoxin (TTX, middle panel, red trace) completely suppresses RTS. Also in paraformaldehyde, which is used to fix the neurons after the recordings, no RTS is observed (PFA, bottom panel, black trace).

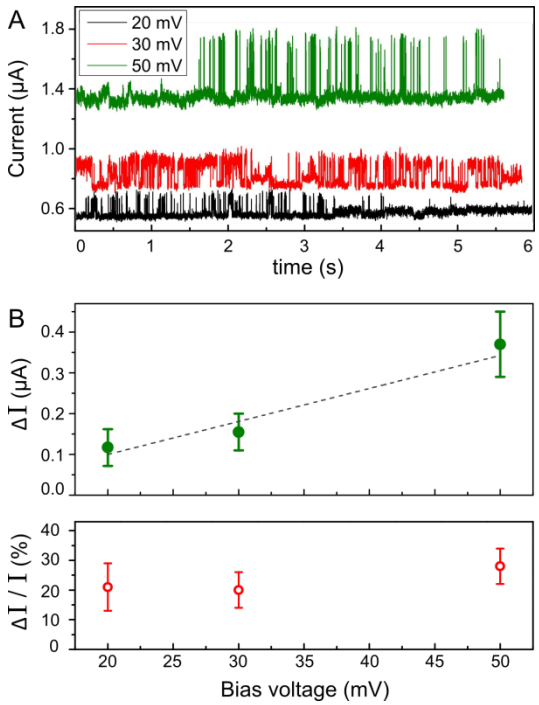

Figure S7. Dependence of RTS amplitude on the bias voltage. (A) Current traces recorded on a 40×50 µm² G-FET interfaced to neurons after 19 days in culture. The recordings were performed in cell culture medium at liquid gate potential set to V_G = 0V using a Pt-electrode and different bias voltages V_{SD} = 20 mV (black trace), 30 mV (red trace) and 50 mV (green trace). (B) While the absolute amplitude of the detected ion channel activity *ΔI* increases with increasing bias voltage (top panel, green dots), the relative signal amplitude *ΔI/I* (bottom panel, red circles) remains nearly constant.

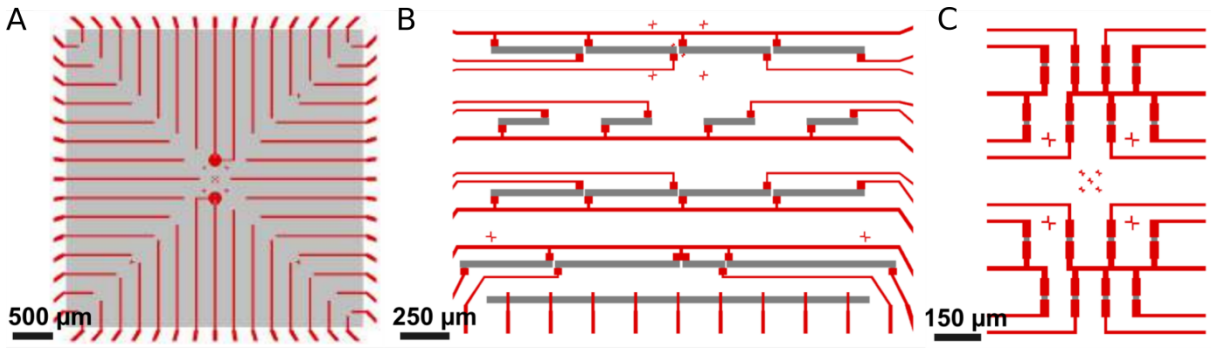

Figure S8. Schematics of the active areas of the several GFETs. (A) The metallic electrodes (red) on the graphene layer (grey) are separated by a distance of 250 µm. (B) 40µm-wide graphene stripes with varying length. (C) GFETs array with 10µm-long and 20µm-wide graphene channels (exposed to the liquid).

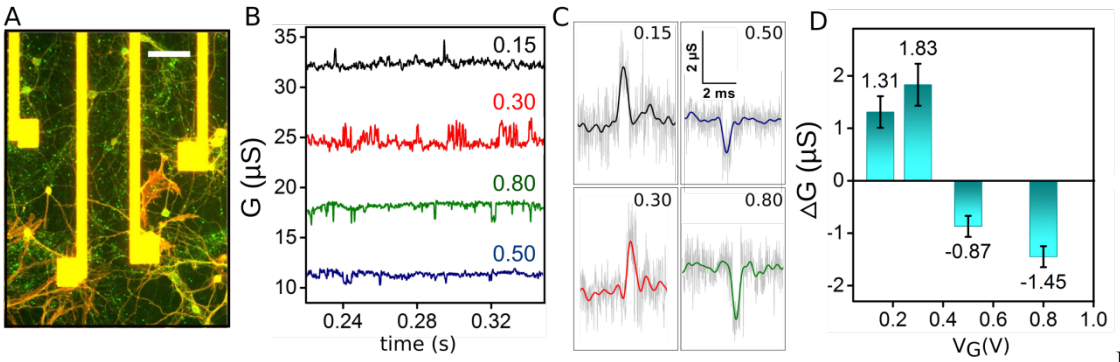

Figure S9. (A) Optical micrograph of neurons (21DIV) on the 40x250µm G-FETs (metallic electrodes appear yellow, phalloïdin and synapsin staining appear red and green respectively (scale bar is 40 µm). (B) Chronograms of the recorded neuronal activity for several gate offsets (V_G = 0.15, 0.3, 0.5, 0.8 V) and (C) extended peaks for the selected gate offsets showing the polarity change while the device is tuned from the p to n branch. (d) Conductance change for the several gate offsets (counted peaks N = 32, 96, 39, 46 respectively). The peak was selected in means of signal duration (equal or above 1 ms).

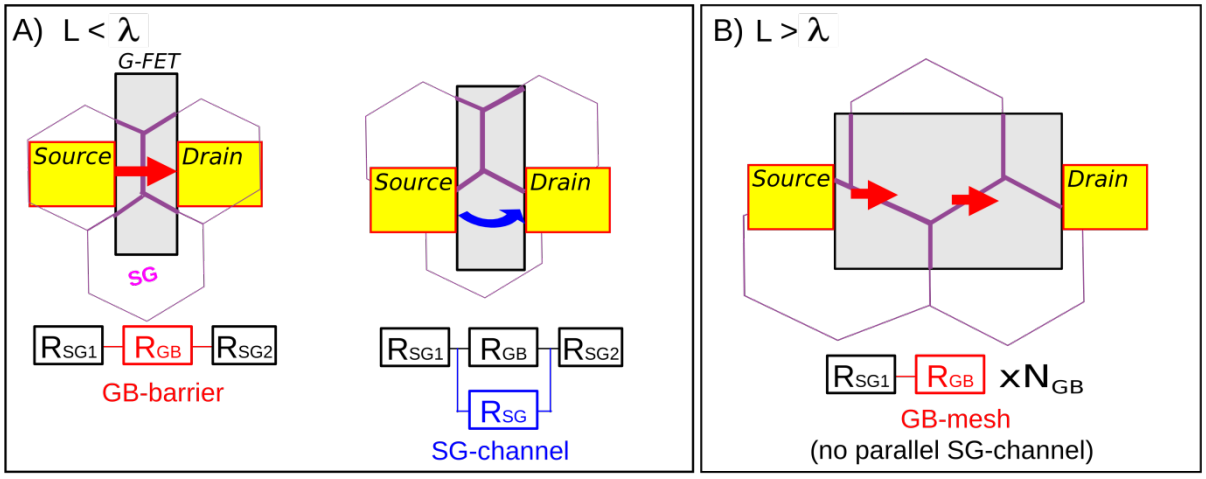

Figure S10. (A) Schematic representation of GBs over the GFET channel, showing the presence of single grain parallel pathways when the size of the GFET is reduced and when the device is not properly aligned such the grain boundary crosses the entire width of the transistor channel. (B) When the dimension of the graphene channel increases, carriers have to overcome the GBs potential barriers. There is no more single grain pathway.